



Growth and electrical properties of $\text{SnS}_{1-x}\text{Se}_x$ ($0 \leq x \leq 1$) single crystals grown using the temperature gradient method

Thi Minh Hai Nguyen¹ · Quang Van Nguyen¹ · Anh Tuan Duong² · Sunglae Cho¹

Received: 29 October 2020 / Revised: 21 December 2020 / Accepted: 21 December 2020 / Published online: 20 April 2021
© The Korean Physical Society 2021

Abstract

Tin selenide (SnSe) has attracted much attention due to its record ZT value in both pristine and doped crystals. This issue has renewed interest in the single-crystal form of tin-based chalcogenide compounds which possess the same layered structure as SnSe such as tin sulfide (SnS). Due to their natural abundances and low toxicities, SnSe and SnS can be alloyed at reduced the processing cost while maintaining the favorable electrical properties of SnSe. In this research, using the temperature gradient method, we successfully fabricated single crystals of $\text{SnS}_{1-x}\text{Se}_x$ with $0 \leq x \leq 1$. High-quality crystals were obtained, and the electrical properties of those crystals were investigated. The results showed that the p-type crystals have layered structures with lattice constants changing gradually according to Vegard's law. The value of the band gap monotonically decreased with increasing Se amount (x). The substitution of Se into S sites results in not only a large increase in the electrical conductivity but also a decrease in the Seebeck coefficient; i.e., the electrical conductivity at room temperature increased from 5×10^{-4} ($x=0$) to $5.24 \text{ S}\cdot\text{cm}^{-1}$ ($x=0.8$). The Seebeck coefficient decreased from 1069 in SnS to $525 \mu\text{VK}^{-1}$ in $\text{SnS}_{0.2}\text{Se}_{0.8}$ and to $481 \mu\text{VK}^{-1}$ in SnSe at room temperature. This work provides positive information for the growth of large-size SnS–SnSe single crystals.

Keywords Single crystals · Tin sulfide · Tin selenide · Electrical synthesis

1 Introduction

Single crystals are widely used in the high-performance optics and semiconductor industry because of their low optical loss and excellent electrical conductivity [1]. A slow directional solidification of the melt, typically the Bridgman method, has been employed to prepare single crystals. The Bridgman method is characterized by placing the crucible containing the melt in an axial temperature gradient in a vertical furnace [2]. This method has an advantage that it can be used in the preparation of large, high-quality single crystals. This conventional method also has disadvantages, for example, low growth rate and high processing cost [2]. Hence, it cannot be directly applied to grow some

challenging compounds, which contain high vapor pressure elements; for instance, tin selenide (SnSe) and tin sulfide (SnS). Both SnSe and SnS show strong anisotropic properties owing to their layered structures [3–5] and are promising candidates for photovoltaic and optoelectronic applications thanks to their proper energy band structure and excellent electronic properties [6, 7]. SnSe has brought about a new breakthrough with a record ZT value of 2.6 at 923 K along its b-axis [8, 9]. Also, because of natural abundance and low toxicity, SnSe and SnS can be alloyed at reduced the processing cost while maintaining the favorable electrical properties of SnSe. Thus, single crystals of SnS, SnSe and their solid solution have attracted tremendous scientific attentions. However, obtaining high-quality SnSe and SnS single crystals in a cheap and convenient way is a challenge. A few efforts have succeeded so far in growing single crystals of SnS, SnSe and their solid solution [8–18]. However, developing a simple and effective growth method to grow large-size, high-quality single crystals is still a challenging issue, so a low-cost and effective method for growing single crystals is needed.

✉ Sunglae Cho
slcho@ulsan.ac.kr

¹ Department of Physics, University of Ulsan, Ulsan 44610, South Korea

² Faculty of Materials Science and Engineering, Phenikaa Institute for Advanced Study, Phenikaa University, Yen Nghia, Ha-Dong district, Hanoi 12116, Vietnam

In this research, we employed a low-cost technique called the temperature gradient method (TGM) to grow $\text{SnS}_{1-x}\text{Se}_x$ ($0 \leq x \leq 1$) single crystals. Our method has advantages over the Bridgman method, such as stable crucibles and low processing cost. In the TGM, the moving parts are absent, and many ampoules can be loaded in one run. The TGM is a low-cost and effective method for the preparation of single crystals. Also, we investigated the electrical properties of in-plane single-crystal samples and the effect of selenide (Se) on the transport properties of tin sulfide (SnS) and discussed the growth and electrical properties of single-crystalline $\text{SnS}_{1-x}\text{Se}_x$.

2 Experiments and discussion

$\text{SnS}_{1-x}\text{Se}_x$ single crystals ($x = 0, 0.2, 0.4, 0.5, 0.6, 0.8, \text{ and } 1$) were fabricated by melting mixtures of high-purity (99.9%) elemental Sn, S, and Se. The three materials were weighted in a molecular ratio of $1:(1-x):x$ and then sealed in evacuated quartz tubes. Then, these tubes were slowly heated to 600°C and then continuously heated to 960°C at 10°C/h , after which they were soaked for 33.3 h to homogenize the melt. In this method, the highest temperature is higher than the crystallization temperatures of SnS and SnSe. Finally, the ampoules were slowly cooled to 600°C and then more rapidly cooled at a rate of 20°C/h to room temperature. The crystals were 35 mm in diameter \times 13 mm in length.

The morphologies of the $\text{SnS}_{1-x}\text{Se}_x$ ($0 \leq x \leq 1$) single crystals were investigated using field emission scanning electron microscopy (FESEM, JEOL JSM—7600F). X-ray diffraction (XRD) measurements were performed using $\text{Cu-K}\alpha$ radiation ($\lambda_{\text{K}\alpha 1} = 1.540598 \text{ \AA}$, $\lambda_{\text{K}\alpha 2} = 1.544426 \text{ \AA}$) (PANalytical X'PERT-PRO). The XRD measurements were carried out on both cleaved crystals and ground powders of the as-grown single crystals. Energy dispersive X-ray spectroscopy (EDS) was used to analyze the elemental composition of each sample. The mass densities of all crystals were determined using the Archimedes method. The ultraviolet–visible–near infrared (UV–Vis–NIR) spectrum was measured at room temperature (Varian, Cary5000). Two bulk specimens were obtained via cutting; one is rectangular-shaped, about $10 \text{ mm} \times 2 \text{ mm} \times 2 \text{ mm}$, for Seebeck coefficient/electrical resistivity measurements and the second one is about $5 \text{ mm} \times 5 \text{ mm} \times 1 \text{ mm}$ for Hall measurement. All properties were calculated along the in-plane direction. The electrical conductivity and the Seebeck coefficient were measured using a physical property measurement system (PPMS) in the temperature range of 20–410 K. The room temperature Hall carrier density n_{H} was calculated from the slope of the V_{H}/I vs. magnetic field curve using the relation $V_{\text{H}}/I = (1/\text{ned})H$, where V_{H} is the Hall voltage, I is the current, n is

the number of carriers, e is the elementary charge, H is the magnetic field, and d is the sample thickness.

The temperature gradient method is described in Ref. [19]. In this method, the crucible is positioned in the furnace, and an increasing temperature profile is imposed along the crucible. The shape of the axial temperature profile is shown in Fig. 1. In this study, Kanthal tape was wound around the furnace, which can be either uniform to obtain an isothermal environment or graded to facilitate gradient freeze growth. An advantage of the temperature gradient method is that both the crucible and the furnace are designed in vertical direction, resulting in a more homogeneous crystal where the melt–solid interface is normal to the growth axis.

At room temperature, each layer of both SnS and SnSe is composed of two-atom-thick structures that run along the b-c plane, and weak van der Waals forces hold these layers together along the a-axis. Figure 2 shows the appearance of crystals, which had a bright metallic luster. The weak van der Waals bonds dominate along the a-axis; hence, the crystals can be easily exfoliated in the b-c plane and all our measurements can be carried out with freshly cleaved surfaces. The morphology, which is determined using SEM, indicates the formation of layered structures for all samples. We observed from the SEM image of the surface structure that grain boundaries, pores, and impurities were absent. Also, the EDS analysis showed that the chemical compositions were similar to the molecular ratio of the prepared materials, as shown in Fig. 2.

To explore the crystal structure of $\text{SnS}_{1-x}\text{Se}_x$, we used X-ray diffraction (XRD). The XRD patterns are presented in Figs. 3a, b. All major sharp diffraction peaks were assigned to low-temperature phases of SnS and SnSe with an orthorhombic structure, as identified using JCPDS card No. 65-6459 for SnSe, 73-1859 for SnS, and 48-1225 for $\text{SnS}_{0.5}\text{Se}_{0.5}$; these samples had no second phases. Additionally, powder XRD data were collected for the phase identification and crystalline parameter determination

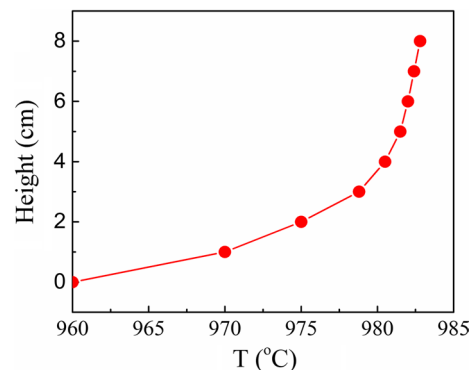


Fig. 1 The temperature distribution for the temperature gradient method (color figure online)

Fig. 2 $\text{SnS}_{1-x}\text{Se}_x$ single crystals: **a** typical as-grown and cleaved crystals and **b** SEM images of $\text{SnS}_{1-x}\text{Se}_x$ single crystals. The subscripts show the compositions determined using EDS

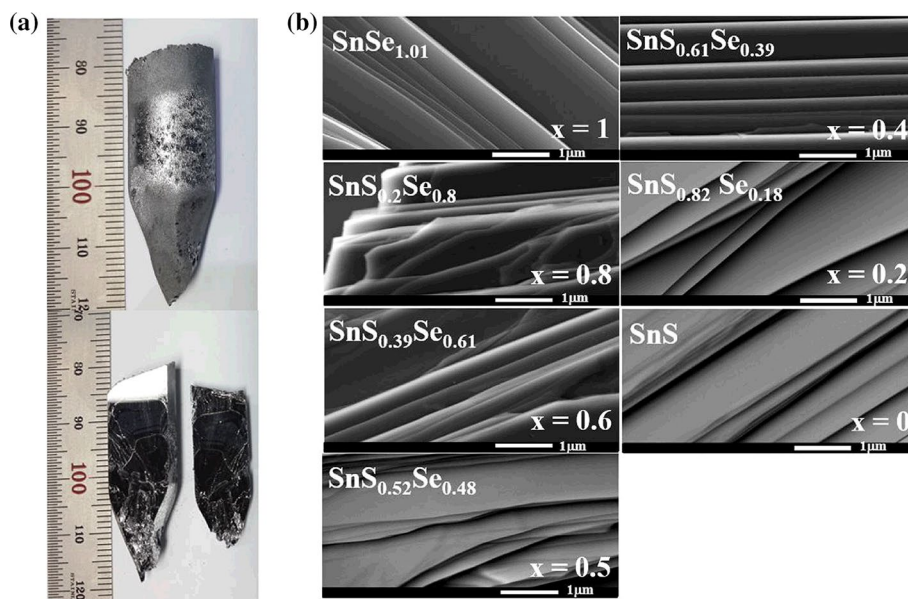
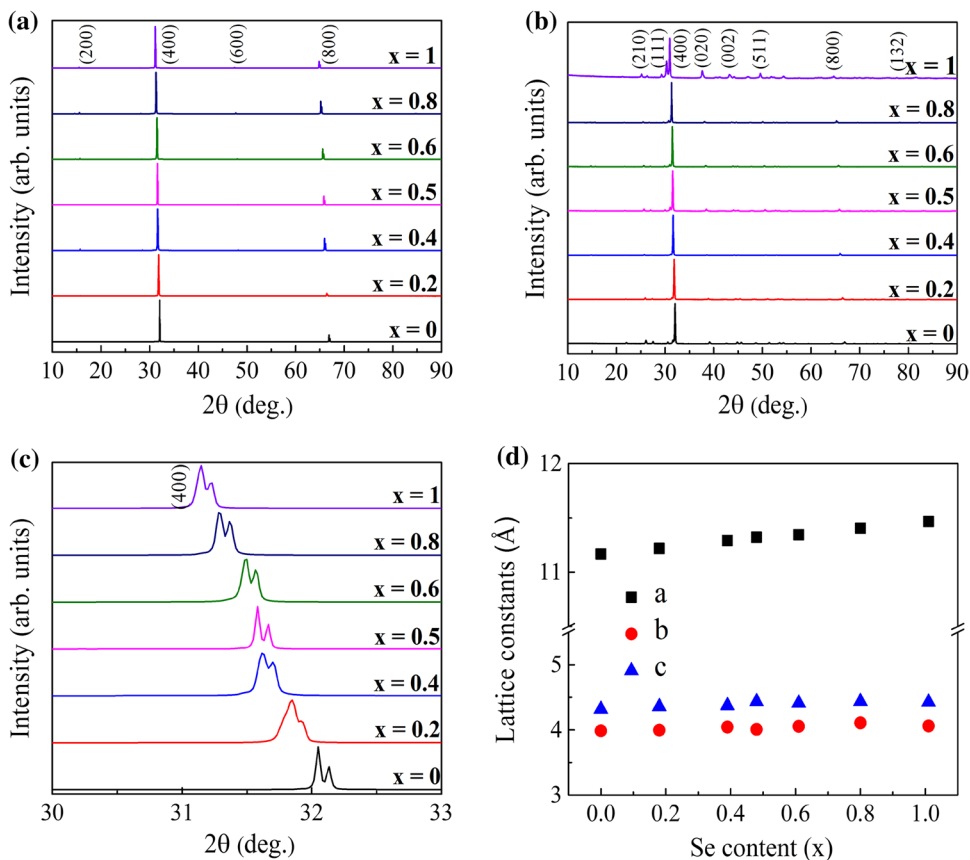


Fig. 3 XRD patterns for $\text{SnS}_{1-x}\text{Se}_x$ single crystals: **a** XRD patterns [20, 25], **b** powder XRD patterns, and **c** the amplification of the strongest (400) diffraction peak. The XRD peaks show a shifting trend with increasing Se alloying fractions [20]. **d** lattice constants for the $\text{SnS}_{1-x}\text{Se}_x$ single crystals [20, 25]. All the above XRD patterns and band gaps indicate that Se was successfully introduced in SnS (color figure online)



(Fig. 3b). The full width at half-maximum (FWHM) of the (400) peak was estimated to be less than 0.06 degree for all samples, as summarized in Table 1. The results show the high quality of the $\text{SnS}_{1-x}\text{Se}_x$ single crystals. The obtained lattice constants (a, b, and c), unit cell volume

and room-temperature densities of the $\text{SnS}_{1-x}\text{Se}_x$ samples are also presented in Table 1. The lattice constants of $\text{SnS}_{1-x}\text{Se}_x$ change gradually with increasing Se content (x) and follow a linear dependence as in Vegard's law, as presented in Fig. 3d. Figure 3c shows that the positions of

Table 1 Lattice parameters derived from the powder XRD pattern, samples' densities and full width at half maximum (FWHM) values of the (400) peaks of all samples

Samples	A (Å)	b (Å)	c (Å)	Volume (Å ³)	Measured mass density (g/cm ³)	(400) peak FWHM (degree)
SnS	11.167	3.986	4.317	192.157	5.15	0.047
SnS _{0.8} Se _{0.2}	11.219	3.995	4.356	195.236	5.34	0.057
SnS _{0.6} Se _{0.4}	11.292	4.044	4.372	199.647	5.60	0.056
SnS _{0.5} Se _{0.5}	11.322	4.008	4.433	201.163	5.63	0.046
SnS _{0.4} Se _{0.6}	11.345	4.055	4.410	202.878	5.64	0.058
SnS _{0.2} Se _{0.8}	11.405	4.108	4.436	207.834	5.88	0.055
SnSe	11.468	4.060	4.426	206.075	5.90	0.048

the diffraction peaks move to a smaller 2θ with increasing of Se content (x) or increasing lattice constants. This variation is a result of the substitution of Se atoms into S-sites. Because the ionic radius of Se (184 pm) is greater than that of S (170 pm), when a larger Se atom is introduced into the position of the smaller S atom, the unit cell expands, leading to an increase in the lattice parameters. This observation proves that a solid solution between SnSe and SnS had completely formed. Furthermore, scanning tunneling microscopy (STM) and first-principles density functional theory (DFT) calculations prove the tendency towards phase segregation into SnSe and SnS of our SnS_{1-x}Se_x [20].

Figure 4 depicts UV–Vis–NIR spectrum and band gap values (E_g) of the SnS_{1-x}Se_x single crystals. The E_g at 300 K was obtained from the $(\alpha h\nu)^{1/2} - h\nu$ plots, as shown in Fig. 4a. The band structure calculations show an insignificant difference in the SnS–SnSe solid solution system [21, 22]. In our work, the E_g of SnS was around 1.162 eV. We observed that, with increasing Se amount, the optical band gap of the solid solution monotonically decreased to 0.95 eV for SnSe, as seen in Fig. 4b. These results are identical to the changing trend in the lattice parameters, which is also reported in Refs. [23] and [24]. In addition,

a systematic study on the polarization dependence of the Raman modes of our single crystals was reported [25].

Figure 5a shows the temperature-dependent electrical conductivity (σ) of all samples. We note that, a pure SnS has a large resistivity value at low temperatures, so data were not available for sub-170 K temperatures. When compared with the pure SnS, the SnS_{1-x}Se_x crystals exhibited a better electrical transport performance. Figure 5a shows a significant improvement in the electrical conductivities after alloying with Se over the entire temperature range. An increase in σ occurs with increasing Se alloying; i.e., at room temperature, σ increase from 5×10^{-4} ($x=0$) to $5.24 \text{ S}\cdot\text{cm}^{-1}$ ($x=0.8$). Thus, the value of σ are four orders of magnitude higher than that of pure SnS. These obtained σ values are comparable to that of the same composition single crystals in Ref. [18] and higher than that of the same composition polycrystalline SnS_{1-x}Se_x [24, 26]. This can be explained by an enhancement in the carrier concentration (n_H). Hall effect measurements were performed along the cleaved plane of the single-crystalline samples. The room temperature n_H increased with increasing fraction of Se, as shown in Fig. 5d. We observed a strong enhancement of the Hall carrier concentration in SnS_{1-x}Se_x with Se contents greater than or equal to 0.6. Sn vacancies lead to p-type characteristics in both SnSe [27] and SnS [28]. In Fig. 5d, at the

Fig. 4 Band gap of SnS_{1-x}Se_x single crystals: **a** UV–Vis–NIR spectrum results, where α is the absorption coefficient, h is the Planck constant, and ν is the frequency and **b** the band gap values. The band gap values decrease with increasing Se fraction (color figure online)

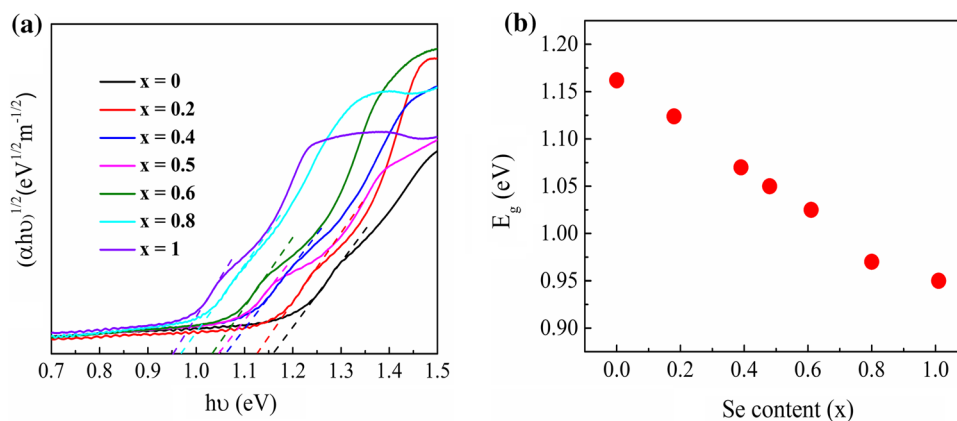
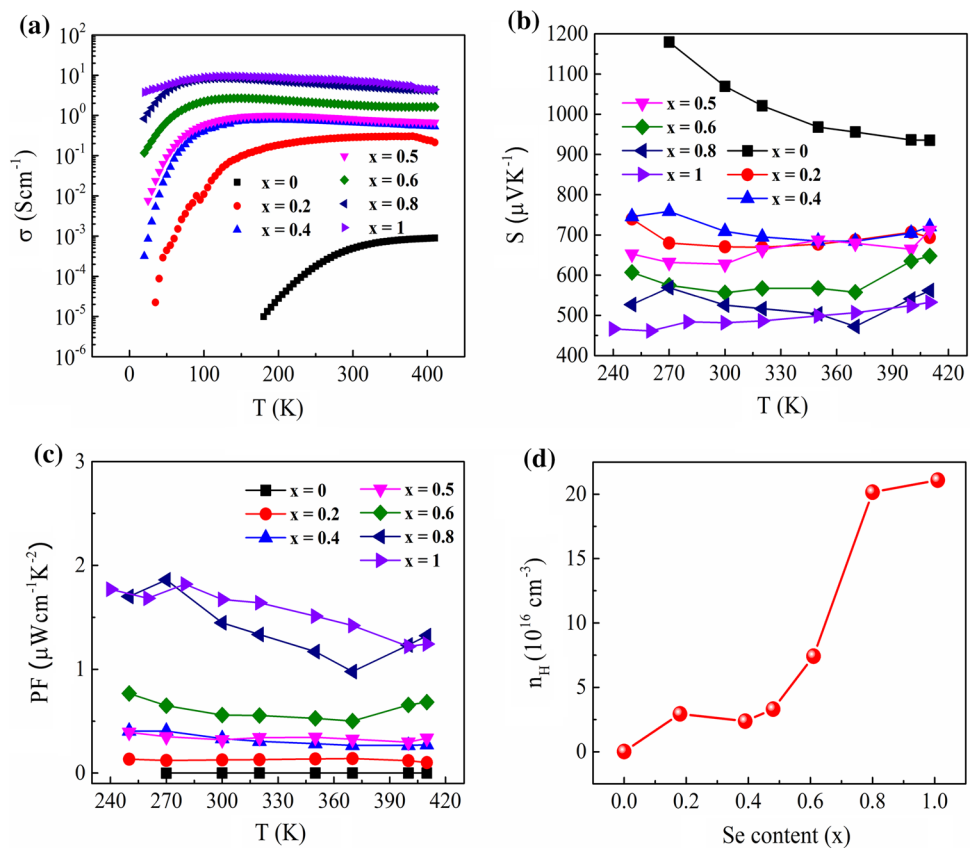


Fig. 5 Electrical transport properties as a function of temperature for $\text{SnS}_{1-x}\text{Se}_x$ crystals: **a** electrical conductivity, **b** Seebeck coefficient, **c** power factor, and **d** Hall carrier concentration of the $\text{SnS}_{1-x}\text{Se}_x$ single crystals versus Se content measured at room temperature (color figure online)



same growth condition, the carrier concentration of SnSe is around two orders of magnitude larger than that of SnS . This observation means that Sn vacancies are more favorable, i.e., easier to be formed in SnSe . As the Se fraction is increased, the size of SnSe cluster formed in $\text{SnS}_{1-x}\text{Se}_x$ increases [20], thus leading to an enhancement of the carrier concentration with increasing x . When x is greater than or equal to 0.6, SnSe becomes dominant; thus, the carrier concentration is strongly enhanced. These results also confirm that the increase in σ by Se alloying results from the enhanced n_{H} . Thus, Se alloying effectively raises the carrier concentration of $\text{SnS}_{1-x}\text{Se}_x$ single crystals.

The temperature-dependent Seebeck coefficients (S) have positive values throughout the temperature range, which confirms the presence of p-type conduction in all samples (Fig. 5b). We observed a decrease in the Seebeck coefficients with increasing Se content from 1069 ($x=0$) to 670 ($x=0.2$), 525 ($x=0.8$), and 481 μVK^{-1} ($x=1$) at room temperature. The Seebeck coefficients decrease as the Hall carrier concentration is increased (Fig. 5d) due to the inverse proportionality between the S and the carrier concentrations [29]. When the improved electrical conductivities and the high Seebeck coefficient are combined, the obtained power factors for the $\text{SnS}_{1-x}\text{Se}_x$ single crystals are much higher than that of pure SnS , as well as polycrystalline $\text{SnS}_{1-x}\text{Se}_x$ [24, 26]. The temperature-dependent power factor

(PF) for all samples is shown in Fig. 5c. The PF is significantly improved with increasing Se content, from $4.12 \times 10^{-4} \mu\text{Wcm}^{-1} \text{K}^{-2}$ for $x=0$ to $1.86 \mu\text{Wcm}^{-1} \text{K}^{-2}$ at 270 K for $x=0.8$, which is even higher than the previously reported value for SnSe [30] while the PF value of our SnSe single crystal is about $1.67 \mu\text{Wcm}^{-1} \text{K}^{-2}$ at the room temperature. These results show that the electrical properties of SnS can be enhanced by alloying it with SnSe due to the increased carrier concentration, thus leading to a high power factor.

3 Conclusion

In summary, high-quality crystalline samples of $\text{SnS}_{1-x}\text{Se}_x$ ($0 \leq x \leq 1$) were successfully synthesized using a temperature gradient method, and the electrical properties of those samples were studied at temperatures below 400 K. The grown samples possessed layered orthorhombic structures. The lattice constants increased with increasing Se content (x) while the optical band gap monotonically decreased. Furthermore, a strong dependence of the carrier concentration on the Se content resulted in large variations of the electrical conductivity and the Seebeck coefficients with Se concentration. Our work indicated that the temperature gradient method is a simple and effective technique for fabricating high-quality and large-size single crystals. Our electrical performance

study of large-sized single crystals could provide a solid research foundation for studying the optoelectronic properties of tin-based binary chalcogenide compounds.

Acknowledgements This work was supported by 2019 Research Fund of University of Ulsan.

References

1. J. Zhang et al., *Adv. Mater.* **2002702** (2020).
2. P. Rudolph (ed.), *Handbook of Crystal Growth* (Elsevier, Amsterdam, 2015)
3. T.H. Patel, R. Vaidya, S.G. Patel, *Bull. Mater. Sci.* **26**, 569 (2003)
4. Z. Tian, C. Guo, M. Zhao, R. Li, J. Xue, *ACS Nano* **11**, 2219 (2017)
5. S. Yang et al., *Nano Res.* **11**, 554 (2018)
6. V.R. Minnam Reddy, S. Gedi, B. Pejjai, C. Park, *J. Mater. Sci. Mater. Electron.* **27**, 5491 (2016)
7. N.K. Reddy, M. Devika, K.R. Gunasekhar, E.S.R. Gopal, *NANO* **11**, 1 (2016)
8. L. Zhao et al., *Nature* **508**, 373 (2014)
9. C. Chang et al., *Science* **360**, 778 (2018)
10. W. He et al., *Science* **365**, 1418 (2019)
11. W. He et al., *J. Mater. Chem. A* **6**, 10048 (2018)
12. A.T. Duong et al., *Nat. Commun.* **7**, 13713 (2016)
13. B.-Z. Sun, Z. Ma, C. He, K. Wu, *RSC Adv.* **5**, 56382 (2015)
14. S.H. Chaki, M.D. Chaudhary, M.P. Deshpande, *Mater. Res. Bull.* **63**, 173 (2015)
15. T.H. Patel, R. Vaidya, S.G. Patel, *High Press. Res.* **23**, 417 (2003)
16. H. Wu et al., *Adv. Energy Mater.* **8**, 1800087 (2018)
17. S. Wang et al., *Appl. Phys. Lett.* **112**, 142102 (2018)
18. K. Peng et al., *Mater. Today* **21**, 501 (2018)
19. V.Q. Nguyen, J. Kim, S. Cho, *J. Korean Phys. Soc.* **72**, 841 (2018)
20. T.T. Ly et al., *Phys. Chem. Chem. Phys.* **19**, 21648 (2017)
21. H. Wei et al., *J. Mater. Chem.* **21**, 12605 (2011)
22. R. Car, G. Ciucci, L. Quartapelle, *Phys. Status Solidi* **86**, 471 (1978)
23. Q. Zhao et al., *J. Solid State Chem.* **273**, 85 (2019)
24. Y.-M. Han et al., *J. Mater. Chem. A* **3**, 4555 (2015)
25. T. Sriv et al., *Sci. Rep.* **10**, 11761 (2020)
26. Asfandiyar et al., *Sci. Rep.* **7**, 43262 (2017)
27. G. Duvjir et al., *Appl. Phys. Lett.* **110**, 262106 (2017)
28. J. Vidal et al., *Appl. Phys. Lett.* **100**, 032104 (2012)
29. G.J. Snyder, E.S. Toberer, *Nat. Mater.* **7**, 105 (2008)
30. F. Serrano-Sánchez et al., *Appl. Phys. Lett.* **106**, 083902 (2015)

Publisher's Note Springer Nature remains neutral with regard to jurisdictional claims in published maps and institutional affiliations.